

Femtosecond laser-induced simultaneous surface texturing and crystallization of a-Si:H thin film: morphology study

Hongliang Wang · Panjawat Kongsuwan · Gen Satoh · Y. Lawrence Yao

Received: 22 August 2011 / Accepted: 5 June 2012 / Published online: 20 June 2012
© Springer-Verlag London Limited 2012

Abstract Hydrogenated amorphous silicon (a-Si:H) thin films have been considered for use in solar cell applications because of their significantly reduced cost compared with crystalline bulk silicon; however, their overall efficiency and stability are less than that of their bulk crystalline counterparts. Limited work has been performed on solving the efficiency and stability issues of a-Si:H simultaneously. Surface texturing and crystallization on a-Si:H thin film can be achieved through one-step femtosecond laser processing, which can potentially alleviate the disadvantages of a-Si:H in solar cell applications. In this study, submicrometer conical and pillar-shaped spikes are fabricated by irradiating a-Si:H thin films deposited on glass substrates with hundreds of 800 nm-wavelength, 130 fs-duration laser pulses in air, and water environments, respectively. The formation mechanisms for the surface spikes are discussed, and the differences in the surface feature characteristics are also presented and explained within the context of the different processing environments. The effect of laser processing on light absorption and crystallinity will be studied later.

Keywords Femtosecond laser · Surface texturing · a-Si:H · Thin film

1 Introduction

Many industrial solar cells in use today use bulk materials as absorbers with crystalline silicon (c-Si) being the most prevalent. Crystalline silicon, however, suffers from the disadvantage of high material cost since relatively large thicknesses are required primarily due to its low absorption coefficient. Recently, thin film absorbers are becoming more attractive based on their potential for low-cost modules, tandem junctions, and large-scale manufacturability [1–3]. a-Si:H is the most popular material for use in thin film form due to its low energy economy (cost per watt). The main issue with a-Si:H is the high order of dangling bonds which act as recombination centers that severely reduce the carrier lifetime which results in the efficiency being below 10 %. Additionally, this initial efficiency will decrease by 50 % or more when exposed to sunlight over a period of several months which is known as the Staebler–Wronski effect or SWE [4, 5].

Due to their low efficiency and instability, thin-film a-Si:H solar cells require a highly efficient light-trapping design to absorb a significant fraction of the incident sunlight and material property changes to increase stability against the SWE. Antireflection (AR) coatings and front-side texturing through the use of alkaline-based solutions, such as KOH and NaOH etching, have been used on crystalline silicon solar cells, and pulsed laser irradiation has been used to enhance light trapping on both amorphous and crystalline materials [6–9], however, AR coating requires additional material and anisotropic wet chemical etching is not applicable for amorphous materials or thin films. In addition, in order to reduce the SWE, hybrid a-Si/nc-Si (nanocrystalline silicon) tandem modules have been developed and are able to achieve both higher efficiency and stability compared with single-junction a-Si:H [10] due to the use of a thinner a-Si layer and the wider

H. Wang (✉) · P. Kongsuwan · G. Satoh · Y. L. Yao
Department of Mechanical Engineering, Columbia University,
Room 220, Mudd Building, 500 West 120th Street,
New York, NY 10027, USA
e-mail: hw2288@columbia.edu

spectral absorption of nc-Si. To eliminate the need for two separate deposition steps which are required to form these tandem cells, laser-induced crystallization of a-Si:H has been proposed to produce a mixture of nc-Si:H and a-Si:H and simultaneously form a light trapping texture on the surface of the material [9]. Therefore, laser-based treatment of a-Si:H may solve its efficiency and stability issues in a one-step process, which is a promising methodology for thin-film solar cell fabrication.

Surface texturing can be achieved by both femtosecond and long-pulse lasers, however, femtosecond lasers are better suited for precise micromachining due to their extremely high peak power and ultrashort pulse duration, which leads to greatly reduced thermal energy diffusion and heat-affected-zone and allows for precise control over the texturing process [11, 12]. Therefore, for texturing films with limited thickness, femtosecond laser processing is more desirable. A number of different techniques have been reported for forming microstructures on silicon surfaces using femtosecond lasers. Mazur et al. [13, 14] showed micron-size conical spikes formed on crystalline bulk silicon when irradiated with hundreds of femtosecond laser pulses in different background gases, such as SF₆, N₂, and air. The formation of submicron spikes and ripples with periodicity in the nano-scale on crystalline silicon has also been investigated after femtosecond laser irradiation in water and has been shown to produce much denser spikes than when processed in a gas environment [15, 16]. Compared with the successful light trapping enhancement achieved on bulk c-Si, limited work has been performed on a-Si:H thin films. Nayak et al. [9] reported the observation of crystallization and simultaneous formation of randomly distributed irregular spikes on a-Si:H thin films through femtosecond laser processing in air. However, the surface geometry created on a-Si:H films is not as regular as that generated on c-Si, and the effects of different processing environments, such as background gases and water, are not well understood. Furthermore, comparing thin film and bulk samples, the processing conditions should be more critical for thin films since the entire film must not be removed during the process. Additionally, based on the difference in thermal properties between amorphous and crystalline materials, the periodicity of the final texture on a-Si:H should be different, especially for underwater treatment.

In this study, a-Si:H thin films deposited on glass substrates are irradiated with different numbers of femtosecond laser pulses at various fluences in air and water, and the formation of conical and pillar-shape spiked surface structure is observed. The feature characteristics are studied through scanning electron microscopy (SEM) and atomic force microscopy (AFM) for different processing environments. The generated surface structure on a-Si:H films shows potential capability of

enhancing the efficiency of thin film solar cells, and the effect of laser processing on absorption and crystallinity is investigated in the later work [17].

2 Theoretical background

2.1 Femtosecond laser interaction with wide-band-gap materials

In this study, the wavelength of the femtosecond laser is 800 nm, which cannot be directly absorbed by a-Si:H (band gap of a-Si:H is 1.7 eV or 730 nm). Therefore, nonlinear absorption is the main laser-material interacting mechanism. When the intensity of the femtosecond laser pulse reaches 10¹³–10¹⁵ W/cm² or more, multiphoton or tunneling ionization will occur within a few to tens of femtoseconds. When the intensity drops below 10¹² W/cm², avalanche (or collisional) ionization which is described by the Fokker–Planck equation occurs [12]:

$$\frac{\partial N(E_K, t)}{\partial t} + \frac{\partial}{\partial E_K} [R_J(E_K, t)N(E_K, t) - \alpha(E_K)E_P N(E_K, t) - D(E_K, t) \frac{\partial N(E_K, t)}{\partial E_K}] = S(E_K, t) \quad (1)$$

where N is the electron density distribution, E_K is the electron kinetic energy, E_P is the phonon energy, t is the time, R_J is the heating rate of electrons, α is the electron–phonon energy transfer to the material, D is the diffusion coefficient and S indicates sources and sinks of electrons. More details of avalanche ionization can be found in Jiang et al. [12].

As the excited electron density increases, the material is first transformed into a plasma that reflects and absorbs the remaining pulse energy. “Gentle ablation”, which is caused by ions being pulled out of the material, can then occur if the electric field formed by the excited electrons is strong enough. This critical electron density, n_{cr} , can be estimated [12]

$$n_{cr} = \frac{\pi m_e c^2}{e^2 \lambda^2} \quad (2)$$

where m_e is the electron mass, c is the speed of light, e is the electron charge, and λ is the laser wavelength.

After the laser pulse, the energy absorbed by the electrons is transferred to the material over a picosecond time scale. Within a few microseconds, the thermal energy of the plasma that diffuses out from the focal volume can cause thermal melting or vaporization and can leave behind permanent structural damage for sufficiently high laser intensities [18, 19].

2.2 Femtosecond laser-induced surface texturing mechanism

Most micromachining work under the ablation regime is performed by removing the material within the irradiated area and generating a crater. However, under some certain conditions, the laser can induce periodic surface structures with periodicity much smaller than the spot size. Extensive work has been performed on femtosecond laser-induced surface texturing of crystalline bulk silicon, and the corresponding two-stage texture formation mechanism has been described by Mazur et al. [15, 20]. During the first stage of processing in a gas environment, straight wavelength-dependent ripple structures are first formed on the silicon surface which is called light-induced periodic surface structure (LIPSS). The ripples are mainly orientated perpendicular to the electric field vector of the incident laser beam and the period can be predicted by [21]:

$$\Lambda \approx \frac{\lambda}{1 \pm \sin \theta_i} \text{ for s-polarized light} \quad (3)$$

$$\Lambda \approx \frac{\lambda}{\cos \theta_i} \text{ for p-polarized light} \quad (4)$$

where, Λ is the spacing between adjacent ripples, λ is laser wavelength, and θ_i is the incident angle. After the formation of LIPSS, micron-scale ridges are generated on the top of and perpendicular to the ripples. The coarsened layer breaks up into micron-size beads which is suggested to be caused by surface tension effects [19]. For a water environment, in the first stage, most of the light is absorbed by a silicon layer tens of nanometers thick near the silicon–water interface which creates a plasma. Due to the high temperature of the plasma, micro-size bubbles are generated by the decomposition of water. Diffraction of the laser beam by these bubbles produces ripple-like structures on the silicon surface due to the existence of high- and low-intensity fringes. The separation between adjacent rings is found to be close to the wavelength of the laser. Roughness on the silicon surface causes the laser pulse energy to be non-uniformly absorbed across the surface, which results in a random arrangement of bubbles. The superposition of ripple structures generated by multiple laser pulses causes bead-like structures to be randomly distributed on the surface of the material.

The second stage of surface structure formation is similar for processing in both gas and water environments. The beads that formed in the first stage act to concentrate subsequent laser light into the valleys between them through reflection off the sides of the

beads. This causes the ablation rate to be higher inside the valleys than on the bead tips, which leads to sharpening of the beads into spikes after hundreds of laser pulse-assisted texturing steps. It is noted that, in water, the spikes are generated with submicron heights and wavelength-dependent spacing and are much shorter and denser than those formed in gas environments.

3 Experimental setup

Amorphous silicon films were deposited on 0.525-mm-thick Corning 1747 glass substrates using plasma enhanced chemical vapor deposition (PECVD). The a-Si:H film was deposited at a rate of 60 Å/s in an hydrogen diluted silane environment at 380 °C with a hydrogen atomic concentration of around 20 %.

Femtosecond laser texturing was carried out using a commercial Ti:sapphire oscillator and regenerative amplifier system. The system delivered 130-fs pulses of linearly polarized light at a 1 kHz repetition rate and a central wavelength of 800 nm. The a-Si:H films were cleaned with acetone in an ultrasonic cleaner for 5 min and then rinsed with methanol and distilled water prior to processing.

The sample was mounted on a three-axis translation stage and irradiated by laser pulses focused by a 60 mm focal-length lens. When changing the environment to water, the sample was placed in a plastic container; the laser beam was focused by the same lens and traveled through 5 mm of distilled water before striking the surface, and the focal plane was positioned below the sample surface in order to obtain the desired spot size of 150 μm. For both air and underwater cases, the laser beam was acting normally to the sample surface, and the beam spot on the sample surface was circular. For the morphology study, the samples were held stationary and irradiated at various fluences (0.2 to 0.45 J/cm²) in air and at higher fluences (1 to 1.8 J/cm²) in water with different numbers of pulses (2–100). At each condition, the experiment had been repeated three times for reliability examination.

The a-Si:H film thickness was measured by ellipsometry at three different locations of each sample wafer, in order to check the uniformity of the PECVD-deposited film. The untreated and treated samples were observed through SEM. Surface roughness and the distribution of spikes in the treated samples were also examined using an AFM. The optical transmittance and reflectance of as received a-Si:H films were measured by a spectrophotometer over a wavelength range of 250–2,500 nm which corresponds to the main spectral range of solar irradiation [22]. The reflectance (R in %) and transmittance (T in %) are then used to calculate the absorbance (A in %) of the film— $A=100-R-T$.

4 Results and discussion

The measured and fitted Psi (Ψ) and Delta (Δ) curves from ellipsometer measurements of the as-received a-Si:H films are shown in Fig. 1. The thickness is determined to be $1,578.6 \pm 2.28$ nm with a surface roughness of 2.62 ± 0.28 nm, where the variation represents standard deviation. These curves were fitted by a numerical model, also shown in Fig. 1, and it is observed that the model generated data matches experimental data well for both number of oscillations and spectral locations.

Figure 2 shows the SEM and AFM images of the initial surface of the a-Si:H film. The surface appears smooth from SEM image, and the surface average roughness measured by AFM is 2.08 nm, which is close to that measured by the ellipsometer. Therefore, the surface of the as-received a-Si:H film is relatively flat with very little initial texture.

4.1 Absorptance spectra of as-received film

The light transmittance and reflectance of a-Si:H thin films are measured by a spectrophotometer, and absorptance can be calculated based on the above two measurements. In this study, a numerical model is also developed to predict the absorptance spectrum of a-Si:H films with planar interfaces, which is used for determining the optical constants, a function of wavelength, of the as-received a-Si:H film, and the determined parameter is helpful for the further-step absorption simulation with a certain periodic surface structures [17]. The model can be also potentially used as a guideline for absorber thickness selection of a-Si:H or other materials if specific optical properties are known. The model configuration consisting of an a-Si:H thin film on a glass substrate as shown in Fig. 3. Since the film thickness is much larger

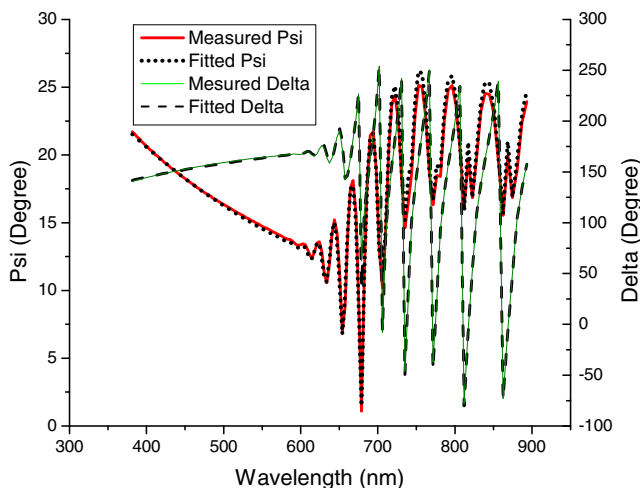


Fig. 1 Comparison of measured and model fitted optical data in the ellipsometer measurement of a-Si:H layer thickness that deposited on glass substrate

than the surface roughness, surface roughness is ignored in the model. This is further justified by the fact that internal interference induced oscillation is observed in the measured transmittance spectrum shown in Fig. 4, which indicates that the thickness of the film is uniform. The light transmittance and reflectance of the a-Si:H thin film are also measured by a spectrophotometer in the solar spectrum of 250 to 2,500 nm, and absorptance is calculated based on the above two measurements as shown in Figs. 4 through 6.

The transmittance through the film/substrate pair can be estimated by considering the light reflection and refraction at the interface between different mediums and the absorption inside the a-Si:H film as below [23]

$$T = \frac{Ax}{B - Cx + Dx^2} \tag{5}$$

where, $A = 16n(s^2 + k^2)$, $B = [(n + 1)^2 + k^2][(n + 1)(n + s^2) + k^2]$, $C = [(n^2 - 1 + k^2)(n^2 - s^2 + k^2) - 2k^2(s^2 + 1)]2\cos\phi - k[2(n^2 - s^2 + k^2) - (s^2 + 1)(n^2 - 1 + k^2)]2\sin\phi$, $D = 2(n - 1)^3(n - s^2)$, $\phi = 4\pi nd/\lambda$, and $x = e^{-4\pi k/\lambda}$

In order to determine optical constants, the method described by Swanepoel et al. [23] is followed which uses the transmittance measurement to determine the optical constants from the interference fringes.

In Fig. 4, within the transparent region, the interference fringes of the model can be written as the maximum and minimum transmittance values for Eq. 5 for $k=0$ [23]

$$T_{\text{peak}} = \frac{A'x}{B' - C'x + D'x^2}, \quad T_{\text{valley}} = \frac{A'x}{B' + C'x + D'x^2} \tag{6}$$

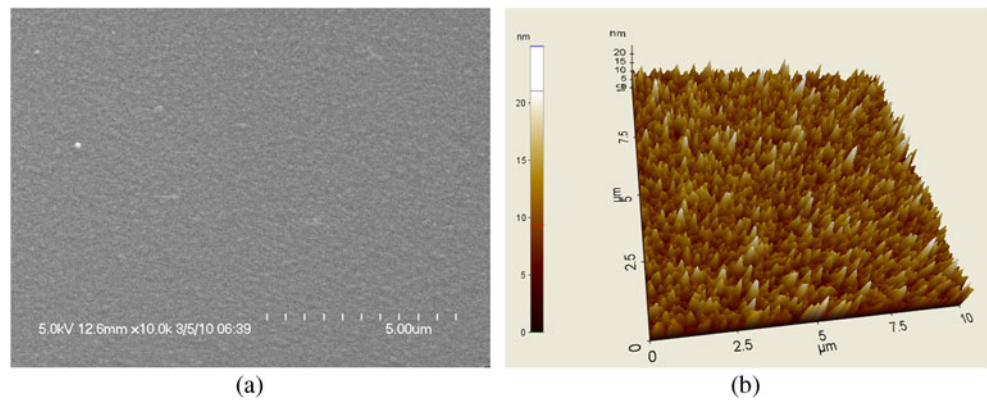
Where $A' = 16ns^2$, $B' = (n + 1)^3(n + s^2)$, $C' = 2(n^2 - 1)(n^2 - s^2)$, and $D' = 2(n - 1)^3(n - s^2)$

The optical constants can be calculated using Eq. 6 at the corresponding wavelengths that cause peaks and valleys, and a polynomial curve fitting of those values gives the optical constants over the solar spectrum. The reflectance can be estimated by the correlation between the light reflection, transmission, a-Si:H absorption coefficient, and film thickness [24]

$$\alpha = \frac{1}{d} \ln \left[\frac{(1 - R)^2 + \sqrt{(1 - R)^4 + 4R^2 T^2}}{2T} \right] \tag{7}$$

The simulation parameters used in the calculation are, substrate refractive index $s=1.5$ and film thickness $d=1,600$ nm. As seen in Fig. 4, the transmittance simulation results show good agreement with the measurement in both

Fig. 2 a SEM image and b AFM image of as-received a-Si:H film surface



periodicity and magnitude. Reflectance curves for both experimental and numerical results in Fig. 5 show that the simulation has the same periodicity as the measurement, however, the simulation values are 10 % to 15 % lower than those measured experimentally. The underestimation could be caused by ignoring the complicated a-Si:H network structure which introduces internal reflections within the film, while the film structure is considered as homogeneous in the model. In addition, ignoring the interface between the glass substrate and the surrounding air in Eq. 7 can also result in a lower reflectance. As a result, the simulated absorptance ($A=100-R-T$) is higher than measured experimentally as shown in Fig. 6, however, the overall wavelength dependence is accurately captured by the model.

4.2 Study of morphology in air

The majority of the published work on femtosecond laser texturing has focused on bulk crystalline silicon, and the texture formation mechanism has been suggested to be quite similar to that of a-Si:H, since both of them occur under the ablation regime. However, in order not to damage the entire film, thin film samples have a much narrower window of suitable texturing fluences and number of pulses than that of bulk materials. Also, for the creation of tandem cells for enhanced stability while maintaining the absorption characteristics of amorphous silicon, crystallization of the entire film must be avoided. This is challenging due to the high absorption coefficient of amorphous silicon and the relatively thin material. Also, the difference morphologies between c-Si and a-Si:H due to the effects on thermal properties and existence of hydrogen are not well studied. Therefore, understand the texturing process of a-Si:H thin films is essential for enabling their widespread use in solar cell applications.

The conditions used to texture crystalline bulk silicon (0.8 J/cm^2 and 500 pulses) [20] easily damage the thin film samples. In order to texture the films without removing them entirely, the amorphous samples are irradiated at stationary locations with lower fluences (0.2 to 0.45 J/cm^2) and numbers of pulses (2 to 100). A typical result achieved using

a fluence of 0.4 J/cm^2 is shown in Fig. 7. The circular surface defects after two pulses as shown in Fig. 7 (a) are suggested to be generated from burst bubbles that are frozen in place on resolidification of the molten silicon. These bubbles are attributed to a local increase in vaporization of the silicon melt due to defects or impurities at the surface [20]. The periodic ripples are suggested to be formed by the interference between the incident beam and light scattered by those surface defects which results in a non-uniform energy distribution on the sample surface, which creates capillary waves with periodicity close to the laser wavelength [25]. Figure 7b shows how the periodic ripples disappear after ten pulses, and instead, perpendicular ridges are formed. The transition could be caused by a surface instability, since the periodic ripples will become long, liquid half-cylinders on the surface after melting; this geometry is not stable if the length of the cylinder is larger than the radius, therefore, the liquid cylinder will be broken into equal-size sections through a process known as cylinder collapse [20]. Some irregular morphology on the surface

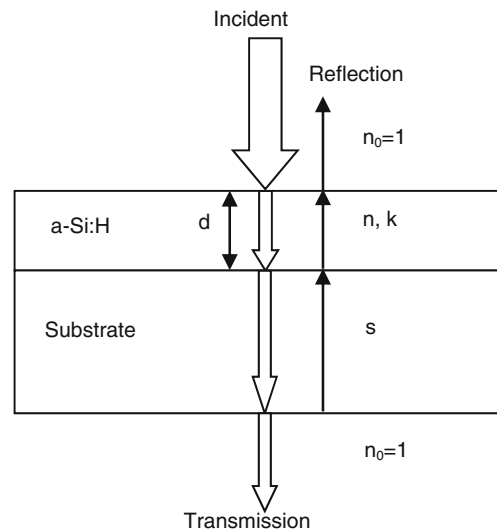
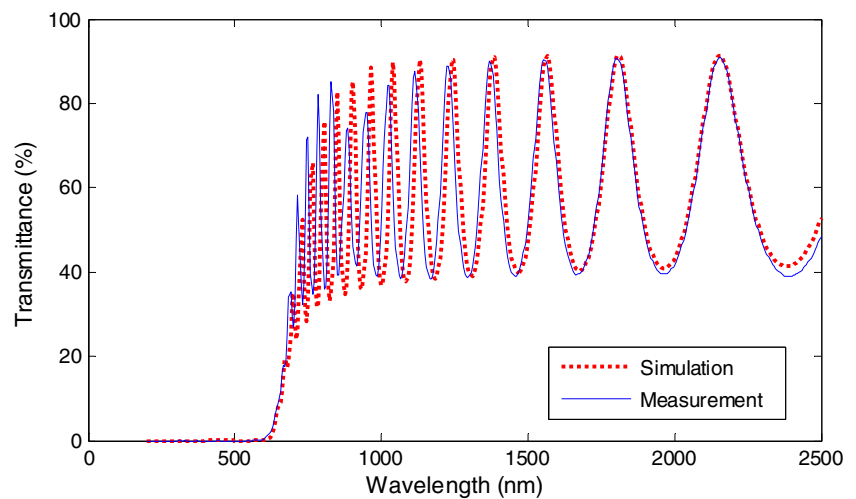


Fig. 3 Schematic of one-dimensional absorption simulation model of as-received a-Si:H film on glass substrate, film thickness $d=1.6 \mu\text{m}$, real and imaginary parts of refractive index of a-Si:H film are n and k , s and n_0 are the refractive index of the substrate and air, respectively

Fig. 4 Comparison of transmittance spectra for both simulation and measurement by spectrophotometer of as-received a-Si:H film on glass substrate



may be caused by the ultrashort pulse duration, which indicates some liquid silicon has been solidified before the surface becomes stable. After 20 pulses, bead-like ripples are formed by breaking those long ridges as shown in Fig. 7c, which is caused by the surface tension effect that is responsible for the shape of liquid droplets. When those droplets start solidifying from the top, this equilibrium status will be broken. The gravity will force the liquid silicon to flow around and this bead-like structure is formed after solidification. The above steps are part of the first stage of texture formation. The following stage is the formation of the conical spikes. Figure 7d and e show how the conical spikes become sharper and deeper with increasing number of pulses. This is due to the beads formed on the surface concentrating the laser beam into the valleys between them, causing the material around the tips to be preferentially removed and sharp conical spikes to be formed. Figure 7f presents the distribution of the spikes in one quarter of the irradiated area. It can be seen that the spikes are wider, taller, and more widely spaced at the center of the laser spot, while they are narrower, shorter, and more closely packed toward the exterior. At the boundary, wavelength-dependent periodic

ripples are formed instead of spikes. This may be due to a difference in surface tension, which mainly depends on temperature and Gaussian spatial distribution of the laser light. The surface tension of liquid silicon is inversely proportional to the temperature [15], thus the liquid silicon at the center more likely has lower surface tension and flows to the surrounding cooler region, and then leaves more sparsely spaced beads after resolidification. When moving to the edge, the increased surface tension will make the beads more compact. Due to the Gaussian distribution of laser energy, the material removal between the beads at the central irradiated area will be more than that of exterior. Therefore, the spikes generated at the center will be higher and less dense than the spikes to the exterior. At the edge, the energy is so small that no further damage can be caused after formation of wavelength-dependent periodic ripples.

In order to study the quantitative characteristics of the feature, AFM measurements are performed. The average spike height and average spike spacing are determined by measuring each spike height above the undamaged material surface, h , and the average distance, d , to the four closest neighboring spikes. A typical condition is 100 pulses at a

Fig. 5 Comparison of reflectance spectra for both simulation and measurement by spectrophotometer of as-received a-Si:H film on glass substrate

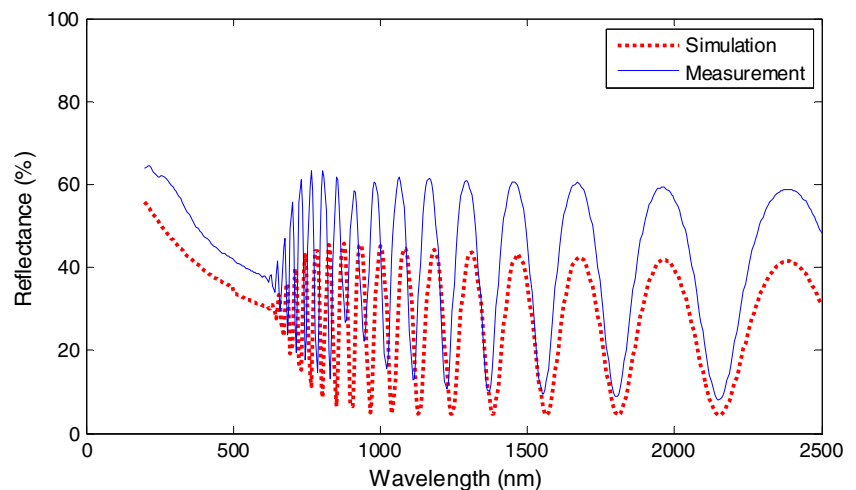


Fig. 6 Comparison of calculated absorptance spectra of as-received a-Si:H film on glass substrate based on both transmission and reflection simulation and measurement by spectrophotometer

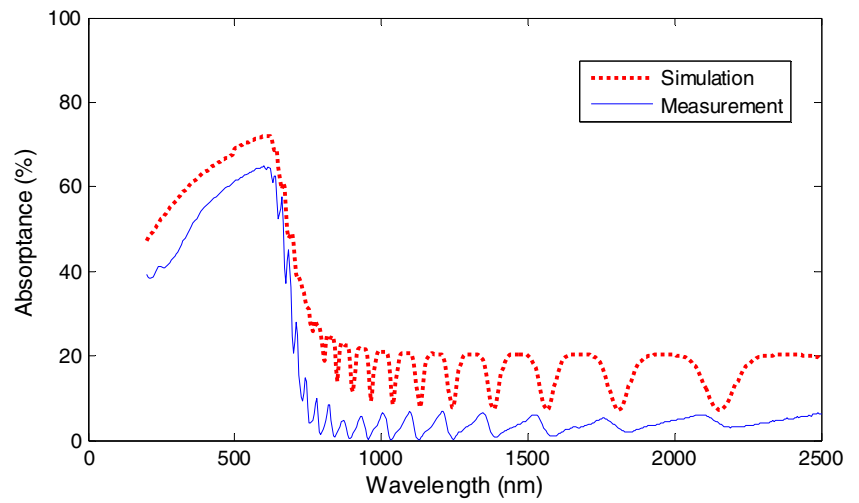
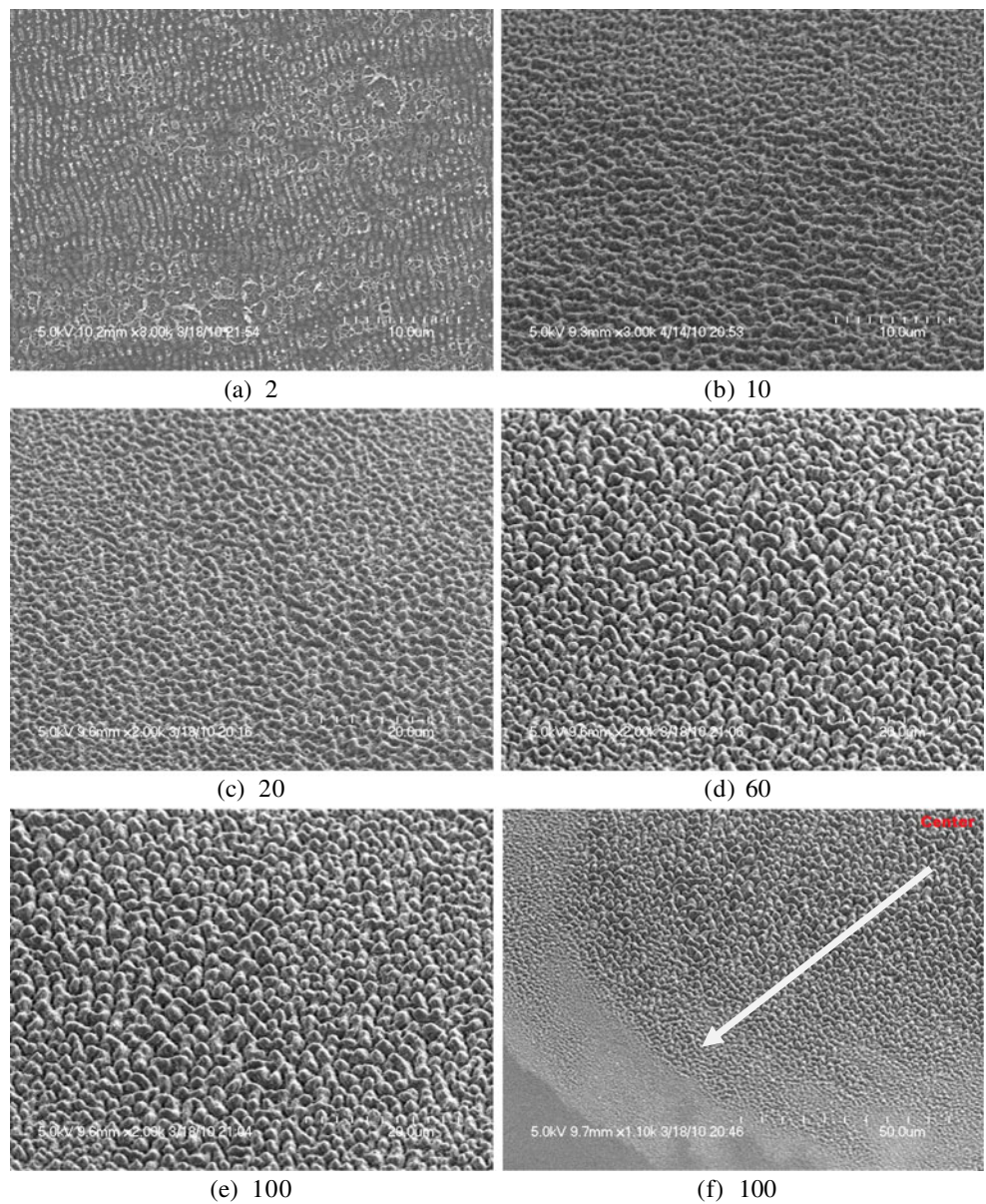
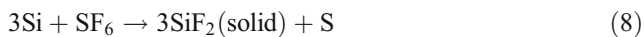


Fig. 7 SEM images of a-Si:H film surface after being irradiated by the following number of pulses in air at 0.4 J/cm^2 **a** 2, **b** 10, **c** 20, **d** 60, **e** 100, **f** 100. With lower magnification, **f** shows about a quarter of irradiated area



fluence of 0.4 J/cm^2 . The average spike height and spacing are measured from within an area of $50 \times 50 \mu\text{m}^2$. Figure 8 shows the average spike height correlated with the average spike spacing, and the variation represents standard deviation. The solid line is a curve fit to the data, yielding a linear relation between the two parameters. When the spacing drops to below $1 \mu\text{m}$, the surface is corrugated with no spikes. Figure 9 shows the average spike spacing within the $50 \times 50 \mu\text{m}^2$ area as a function of fluence when irradiated by 100 pulses, and the variation represents standard deviation. It indicates that higher fluences will lead to an almost linear increase in average spike spacing; therefore, both average spike spacing and height are linearly proportional to the laser fluence, which is different from the nonlinear correlations found for bulk crystalline silicon with the condition variation from 0.5 to 1 J/cm^2 and irradiated at 500 pulses [26]. The reason could be the chemical etching caused by the background gas (SF_6) during the laser irradiation on c-Si. The etching process can be described as: (1) SF_6 reacts with liquid silicon and form SiF_2 compounds; (2) SiF_2 compounds are desorbed by the laser, volatile species leave the surface [27]:



When the spikes start generating, the multi-reflection effect between the spikes introduces more intense laser energy into the valley. More silicon fluoride compounds desorb from the silicon matrix, which leads to a higher

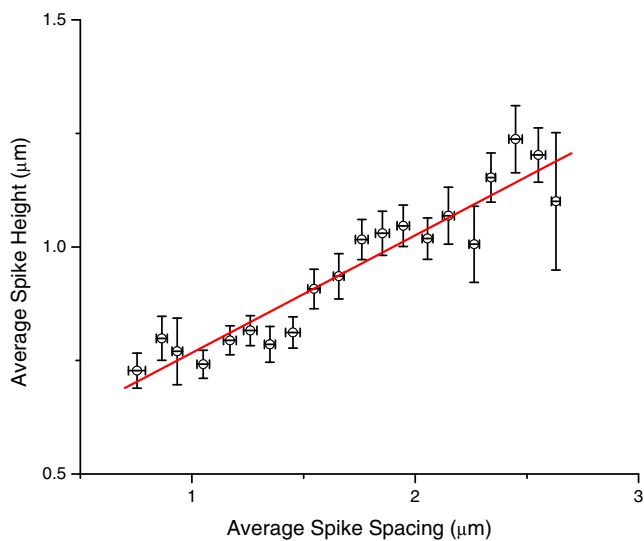


Fig. 8 Dependence of average spike height on average spike spacing after laser treatment in air, determined from an area of $50 \times 50 \mu\text{m}^2$ at the processing center (0.4 J/cm^2 , 100 pulses). The solid straight line is a linear fitting to the measurement, error bars indicate standard deviation

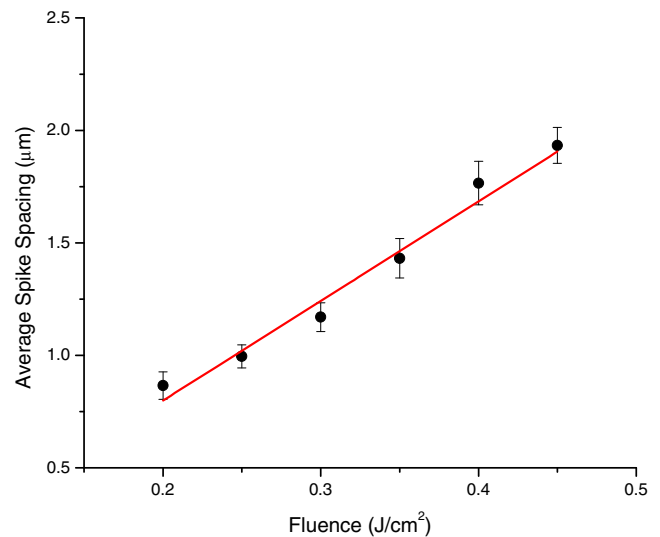
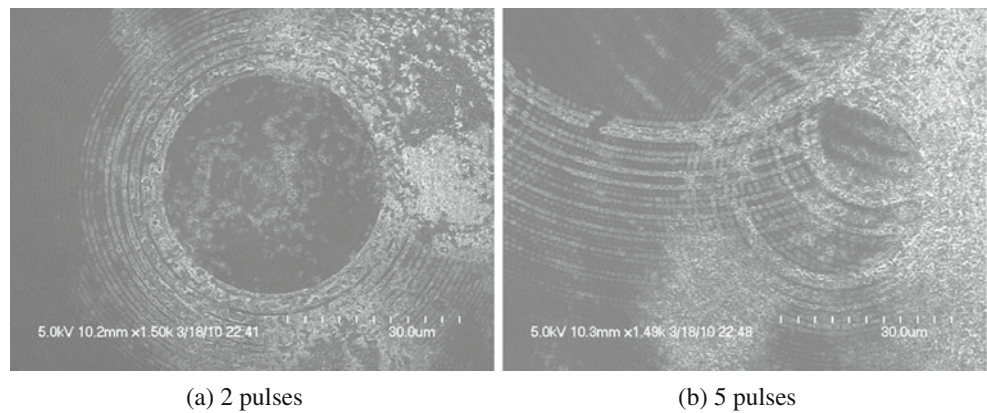


Fig. 9 Dependence of average spike spacing on laser fluence for a fixed number of pulses (100 pulses) after treated in air, determined from an area of $50 \times 50 \mu\text{m}^2$ at the processing center. The solid straight line is a linear fitting to the measurement, error bars indicate standard deviation

ablation rate. Thus the higher the fluence, the more chemical reaction happened between the silicon and SF_6 . Therefore, beyond the dependence on the laser fluence, the chemical reaction also plays an important role of the spike formation, which may cause the nonlinear relationship between the average spike height and spacing and the laser fluence.

As shown in Carey et al. [28], when irradiating on c-Si with a fluence of 0.4 J/cm^2 and 500 pulses, the c-Si surface cannot generate sharp spikes, but only bead-like structures with an average spacing of $3.5\text{--}4 \mu\text{m}$. However, under the same fluence but 100 pulses, the average spacing is $1.8 \mu\text{m}$ on a-Si:H surface. Bases on the interaction mechanism of femtosecond laser, the material starts being ablated, and then thermal vaporization occurs when the energy transfers back from free electrons to the material. Finally, the remaining energy induces thermal melting underneath the ablation layer. Although the melting temperature of dehydrogenated amorphous silicon (a-Si) is around $250 \text{ }^\circ\text{C}$ below that of c-Si [29], the existence of hydrogen can significantly decrease the vaporization temperature (the energy of evaporation of H is four orders of magnitude lower than that of Si). Therefore, the energy absorbed by a-Si:H for melting will be less than that of c-Si, so that under the same fluence, the temperature of liquid silicon in a-Si:H sample is lower. As discussed in Fig. 7f, the higher the temperature, the lower the surface tension, and the larger the spike spacing. That is why the average spike spacing of a-Si:H is smaller than that of c-Si. Her et al. [26] also shows that, for c-Si sample processed at a higher fluence (1 J/cm^2) and number of pulses (500), when the spike spacing is around $2 \mu\text{m}$, the average spike height is $0.8\text{--}0.9 \mu\text{m}$, which is close to that of a-Si:H

Fig. 10 SEM images near the edge of underwater laser irradiation area on a-Si:H film for **a** 2 pulses **b** 5 pulses at the fluence of 1.4 J/cm^2



sample (Fig. 8). This may be also caused by the influence of hydrogen. Elliq et al. [30] shows that, under the same condition, the surface roughness of a-Si:H can be several times as that of a-Si sample. The reason is that the hydrogen atoms can be aggregated together by absorbing laser energy, and finally, the hydrogen is formed as gaseous phase and diffused out from the silicon matrix. Since the ablation thresholds of both a-Si and c-Si are around 0.2 J/cm^2 [31], under the same fluence, the ablation rate of a-Si:H could be more than that of c-Si. Therefore, with a smaller fluence (0.4 J/cm^2) and number of pulses (100), a-Si:H sample can generate similar spike height to that of c-Si. Actually, the surface morphology can also be affected by other factors, such as melt depth, cooling rate, and pressure. However, based on the formation process shown in Fig. 7, the average spike spacing is mainly caused by thermal effect of the melting layer at the first stage when bead-like structure is formed. The average spike height mainly depends on the ablation rate of the material and the influence of background gases. Similar to c-Si [26], the laser textured spikes on a-Si:H

should be at or below the original surface since it is ablation-based laser processing. In opposite, the spikes are protruded from the original surface using a nanosecond laser where thermal effect is dominant during the spike formation [20]. Although the remaining energy can cause a thin-layer of molten material, the molten layer has a relative minor effect on spike height.

Compared with Nayak et al. [9], this study can generate much more regular conical spikes, which are similar as those achieved on bulk c-Si. Therefore, with a better periodic structure, the potential of absorption could be also better than that of Nayak et al. [9].

4.3 Further study of morphology in water

After laser processing, the top layer of the material will become oxidized, which has a larger band gap than a-Si:H and is not desirable for solar cell absorbers; the use of a water layer, however, may be introduced to reduce the surface oxidation and eliminate debris redeposition. The

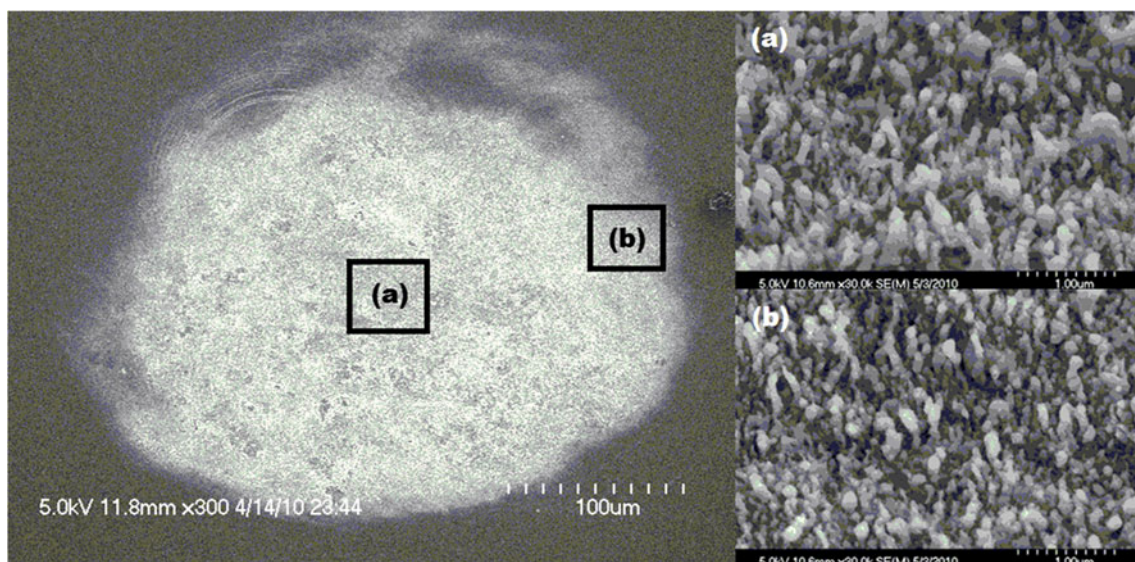
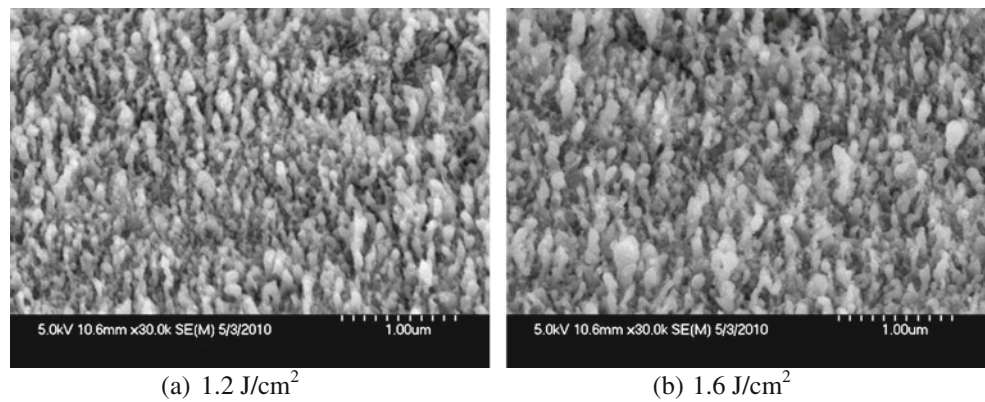


Fig. 11 SEM images of underwater laser irradiation of a-Si:H film for 50 pulses at fluence of 1.4 J/cm^2 , the irradiation spot diameter is $150 \mu\text{m}$, the inset images in the right show the high magnification at the center (a) and edge (b)

Fig. 12 SEM images of underwater laser irradiation of a-Si:H film for 50 pulses at fluence of **a** 1.2 **b** 1.6 J/cm²



difference in surface stability between liquid silicon and water compared with air may also allow for different spike geometries. During laser processing, the plasma generated at the silicon/water interface due to the high temperature can vaporize and decompose the water, since some of the large bubbles can still be observed after irradiation when the temperature goes down to room temperature, so that they must consist primarily of gaseous hydrogen and oxygen rather than water vapor. The energy absorbed by the bubbles and the scattering effects induced by these bubbles and suspended ablated material will cause part of the incident energy to be lost before it reaches the target. Daminelli et al. [16] shows the ablation threshold for 100-fs laser pulses of c-Si in water is around 1.5 times that in air, and also that periodic ripples are formed in water when irradiated at fluences of 1.5–1.6 J/cm², which indicates that the incident energy in water needs to be higher in order to get similar energy on the target. Therefore, for the a-Si:H surface processed in water, the sample is irradiated at stationary locations with higher fluences (1 to 1.8 J/cm²) than that in air and the same number of pulses (2 to 100).

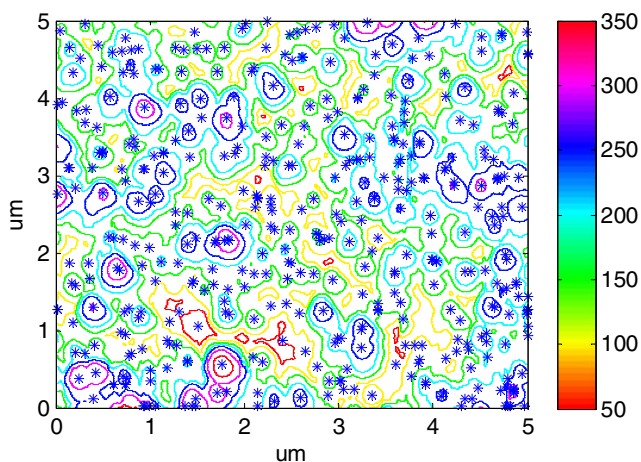


Fig. 13 Schematic of peak identification of extraction data from AFM images of underwater laser irradiated a-Si:H film at different fluence and number of pulses, *asterisks* indicate the identified peak point, *solid curves* indicate the contour spectra, AFM scanning area is 5×5 µm, color bar unit: nanometers

Figure 10a and b show SEM images taken near the edges of the laser irradiated spot on an a-Si:H film surface after 2 and 5 pulses, respectively, with a fluence of 1.4 J/cm², and the spot diameter is 150 µm. It can be seen that a ripple-like structure is generated on the surface after 2 pulses due to diffraction of the laser light by the micro-bubbles and that the spacing between the adjacent rings is closely matched to the laser wavelength (800 nm). The first pulse cannot bring the ripple formation (not shown) is because no bubbles existence at the beginning. The laser energy is absorbed by the plasma at the silicon/water interface, and the heat of generated vapor and decomposed bubbles required may cool the silicon surface locally and leave the damage on the surface. After 5 pulses, at the edge of the irradiation area, it can be seen that ripples diffracted by separated bubbles start overlapping and generate a wavelength-dependent bead-like structure. When moving to the center of the area, the surface consisting of small spikes which are similar to those shown in Fig. 11a suggests that more ripples are overlapping near the center of the beam, due

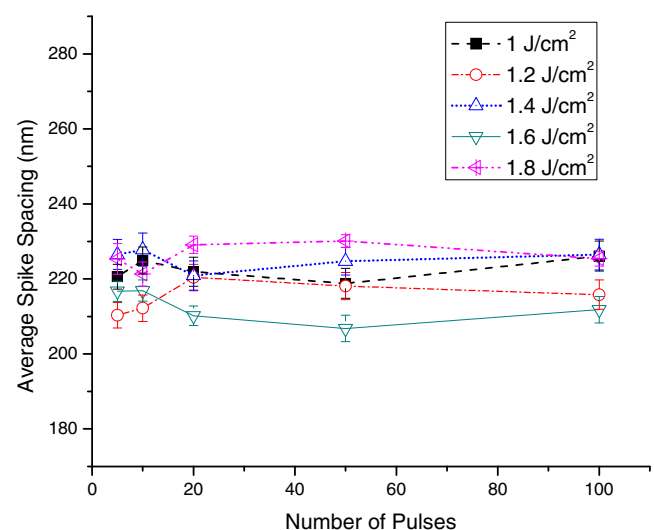


Fig. 14 Dependence of average spike spacing on laser fluence and number of pulses in water, error bars indicate standard error

to higher intensity in the center of the Gaussian beam that causes more decomposition of water and a greater number of bubbles to form. Figure 11 shows the entire 50-pulse irradiated spot processed at a fluence of 1.4 J/cm^2 . The inset images (a) and (b) show that the spikes formed at the center and the edge are very similar, which indicates that after 50 pulses, the entire irradiated area looks more uniform and the ripples have disappeared. Instead, nano-sized pillar-shaped spikes are formed on the surface, which look less regular and denser but are more uniformly distributed than those formed in air shown in Fig. 7. Figure 12a and b show SEM images of the surfaces irradiated by 50 pulses at fluences of 1.2 and 1.6 J/cm^2 , respectively. Compared with Fig. 11, the spikes formed in water at different fluences look quite similar. This is due to the surface instability effect influenced by water confinement that will be discussed later.

In order to further understand the correlation between spike formation and fluence, AFM images were taken at the center ($5 \times 5 \text{ }\mu\text{m}^2$) of samples irradiated by different fluences and numbers of pulses, and then the average spike height and spacing were calculated. In order to obtain reasonable estimate for the non-uniform spike morphology, peak identification from the AFM data was performed by first applying a smoothing filter in order to eliminate the labeling of small height fluctuations as peaks. The peak positions were determined by finding points where the first-order derivative is zero and second-order derivative less than zero. A typical result is shown in Fig. 13, where asterisks indicate peak positions. The average distance to the four closest peaks is determined for each peak, and the average spacing between the peaks can then be estimated. Figure 14 shows that the average spike spacing is nearly constant for different fluences and number of pulses. Considering the imperfect spike distribution, this small variation range of 210–230 nm suggests that the separation between the spikes is stable at around 200 nm, and it is much smaller than the wavelength-dependent ripples formed at the beginning of irradiation. A similar phenomenon has been shown by Daminelli et al. [16], the ripples generated on crystalline bulk silicon with both wavelength-dependent and much smaller ($\sim 100 \text{ nm}$) spacing are observed after 100 pulses irradiation at a fluence of $1.5\text{--}1.6 \text{ J/cm}^2$, and only 100 nm periodicity structures left after 1,000 pulses. They suggested that this smaller spacing could be due to surface energy effects between the molten silicon and water which stabilizes more tightly spaced ripples. This may indicate that the a-Si:H surface will be unstable after superposition of the wavelength-dependent ripples and further self-assembly processes make the surface stabilize at much smaller-spaced spikes. The larger spacing of 200 nm compared with the crystalline samples textured

in water may be caused by differences in the physico-chemical properties [32] between a-Si:H and c-Si, which indicates that a-Si:H may have a larger surface energy during processing such that the larger-spacing spikes are formed by a larger driving force. It is noted that Shen et al. [15] showed regular spikes with wavelength-dependent spacing generated on a c-Si surface by irradiating hundreds of pulses at a fluence of 0.76 J/cm^2 . This shows that the surface can be stable after superposition of different diffracted ripples if the fluence is low enough and the self-assembly process does not occur. It may suggest that the self-assembly process has a “threshold”, such that at a fluence lower than the “threshold” the smaller-spaced surface structures will not be formed. As discussed above, this threshold is much lower for a-Si:H than for c-Si, which could be caused by different optical properties between the different materials. Since the molten surface of both a-Si:H and c-Si are the same, i.e., liquid silicon, the surface temperatures at this “threshold” of both materials must be equal. a-Si:H will absorb more energy than c-Si after the same number of laser pulses at the same fluence, and the higher temperature distribution on the a-Si:H surface causes it to have a lower threshold to re-assemble the molten surface during solidification.

In Fig. 15, it can be seen that for the fluences of 1, 1.2, and 1.4 J/cm^2 , the average spike heights linearly increase with increasing fluence and number of pulses up to about 50 pulses. Due to the bead-like structure concentrating the light and causing the ablation rate beside the beads to be higher than that on the tips, the spikes are formed increasingly higher. After a few tens of pulses, the average height goes to a maximum which means that material between the spikes has been completely removed, therefore, the subsequent laser pulses start reducing the height of the spikes because

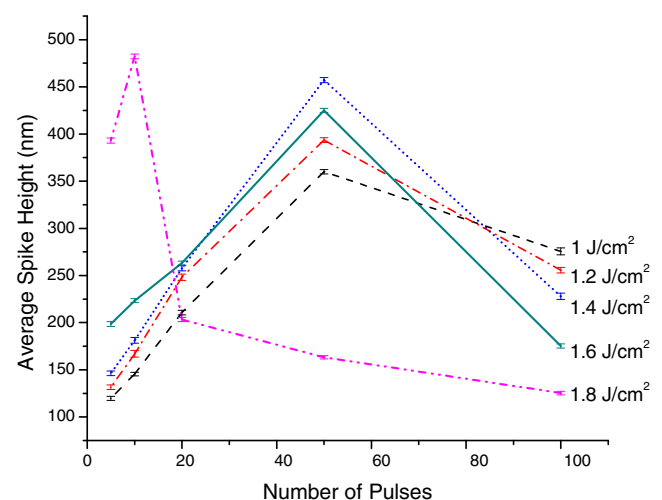


Fig. 15 Dependence of average spike height on laser fluence and number of pulses in water, error bars indicate standard error

the pulses only remove the material at the tips and the energy is not high enough to damage the substrate. This causes the average height of spikes after 100 pulses to be lower than that at 50 pulses. The tallest spikes after 100 pulses are formed for the lowest fluence of 1 J/cm^2 since the ablation rate is proportional to fluence, resulting in the least spike tip ablation. At the higher fluences of 1.6 and 1.8 J/cm^2 , the average peak heights follow the same overall trend with number of pulses as the lower fluences. However, the spike height after 50 pulses at 1.6 J/cm^2 is less than that when processed at 1.4 J/cm^2 , which means the spike height has already started decreasing by 50 pulses at 1.6 J/cm^2 . For an even higher fluence of 1.8 J/cm^2 , the point at which full-film-depth ablation occurs is after only 10 pulses, and the significantly reduction in peak height after 20 pulses indicates that nearly the whole film has been removed. The reason why the substrate between the spikes cannot be clearly seen in Fig. 12b may be due to the re-deposition of ablated material. However, if the sample is irradiated by hundreds of pulses, it will be clear that the film has been fully removed at the center of the irradiated area (not shown).

5 Conclusion

In conclusion, it has been demonstrated that the surface texturing of a-Si:H thin films is able to be achieved by irradiation by multiple femtosecond laser pulses in both air and water environments. Furthermore, the formation of spikes on laser irradiated a-Si:H surfaces in air follows a similar mechanism to crystalline bulk silicon, however, compared with bulk silicon, a-Si:H thin film have a narrower processing window for suitable texturing fluences in order to not damage or crystallize the entire film. The average spike spacing and height is proportional to the laser fluence, and the spikes are taller, wider, and more sparsely distributed at the center than those at the exterior due to the spatial Gaussian distribution of the laser pulses. In water treatment, unlike the formation of wavelength dependent spikes or 100 nm-spacing periodic ripples on crystalline bulk silicon, pillar-shaped spikes are generated on a-Si:H film surfaces with an average spike spacing of around 200 nm. This has been suggested to be caused by the presence of water that influences the interface and the stabilization of more tightly spaced ripples. The average spike height formed in water increases linearly with laser fluence and number of pulses until the material between the spikes is completely removed, after which the opposite trend is observed. Finally, the surface texturing is suggested to improve the absorbance over the

entire solar radiation spectrum, which indicates that femtosecond laser processing may allow for the fabrication of more efficient and economical a-Si:H thin film absorbers than currently achievable through crystalline bulk silicon for solar cells applications.

Acknowledgment Research carried out in part at the Center for Functional Nanomaterials, Brookhaven National Laboratory, which is supported by the US Department of Energy, Office of Basic Energy Sciences, under Contract No. DE-AC02-98CH10886. The use of material characterization equipment at Materials Research Science and Engineering Center, Columbia University is gratefully acknowledged. The authors also would like to thank Prof. Vijay Modi, Department of Mechanical Engineering, Columbia University, for helpful discussion and suggestions.

References

1. Luque A, Hegedus S (2003) Handbook of photovoltaic science and engineering. Wiley, UK, Chapter 7-8
2. Chopra KL, Paulson PD, Dutta V (2004) Thin-film solar cells: an overview. *Prog Photovolt: Res Appl* 12:69–92
3. Kazmerski LL (2006) Solar photovoltaics R&D at the tipping point: a 2005 technology overview. *J Electron Spectrosc Relat Phenom* 150:105–135
4. Miles RW, Hynes KM, Forbes I (2005) Photovoltaic solar cells: an overview of state-of-the-art cell development and environmental issues. *Prog Cryst Growth Charact Mater* 51:1–42
5. Staebler DL, Wronski CR (1980) Optically induced conductivity changes in discharge-produced hydrogenated amorphous silicon. *J Appl Phys* 51(6)
6. Martirosyan KhS, Hovhannisyanyan AS, Arouiounian VM (2007) Calculation of reflectance of porous silicon double-layer antireflection coating for silicon solar cells. *Phys Status Solidi (C)* 4(6):2103–2106
7. Hylton JD, Burgers AR, Sinke WC (2004) Alkaline etching for reflectance reduction in multicrystalline silicon solar cells. *J Electrochem Soc* 151(6):G408–G427
8. Crouch CH, Carey JE, Warrender JM, Aziz MJ, Mazur E, Genin FY (2004) Comparison of structure and properties of femtosecond and nanosecond laser-structured silicon. *Appl Phys Lett* 84(11):1850–1852
9. Nayak BK, Gupta MC (2007) Femtosecond-laser-induced-crystallization and simultaneous formation of light trapping microstructures in thin a-Si:H films. *Appl Phys A* 89:663–666
10. Yamamoto K et al (2004) A high efficiency thin film silicon solar cell and module. *Sol Energy* 77:939–949
11. Zheng HY, Jiang ZW (2010) Femtosecond laser micromachining of silicon with an external electric field. *J Micromech Microeng* 20:017001
12. Jiang L, Tsai HL (2003) Femtosecond laser ablation: challenges and opportunities. *Proceeding of NSF Workshop on Research Needs in Thermal, Aspects of Material Removal*, Stillwater, OK, 163–177
13. Younkin R, Carey JE, Mazur E, Levinson JA, Friend CM (2003) Infrared absorption by conical silicon microstructures made in a variety of background gases using femtosecond-laser pulses. *J of Applied Physics* 93(5):2626–2629
14. Sheehy MA, Winston L, Carey JE, Friend CM, Mazur E (2005) Role of the background gas in the morphology and optical properties of laser-microstructured silicon. *Chem Mater* 17:3582–3586

15. Shen MY, Crouch CH, Carey JE, Mazur E (2004) Femtosecond laser-induced formation of submicrometer spikes on silicon in water. *Appl Phys Lett* 85(23):5694–5696
16. Daminelli G, Kruger J, Kautek W (2004) Femtosecond laser interaction with silicon under water confinement. *Thin Solid Films* 467:334–341
17. Wang H, Kongsuwan P, Satoh G, Yao YL (2012) Femtosecond laser-induced simultaneous surface texturing and crystallization of a-Si:H thin film: absorption and crystallinity. *J Manuf Sci Eng* 134:031006
18. Gattass R, Mazur E (2008) Femtosecond laser micromachining in transparent materials. *Nat Photonics* 2:219–225
19. Sundaram SK, Mazur E (2002) Inducing and probing non-thermal transitions in semiconductors using femtosecond laser pulses. *Nat Mater* 1(4):217–224
20. Tull BR, Carey JE, Mazur E, McDonald JP, Yalisove SM (2006) Silicon surface morphologies after femtosecond laser irradiation. *MRS Bull* 31(8):626–633
21. Tan B, Venkatakrishnan K (2006) A femtosecond laser-induced periodical surface structure on crystalline silicon. *J Micromech Microeng* 16:1080–1085
22. Goetzberger A, Knobloch J, Voss B (1998) *Crystalline silicon solar cells*. Wiley, Chichester, Chapter 2
23. Swanepoel R (1983) Determination of the thickness and optical constants of amorphous silicon. *J Phys E Sci Instrum* 16:1214–1222
24. Shaaban ER (2008) Calculation of optical constant of amorphous germanium arsenoselenide wedge-shaped thin films from their shrunk transmittance and reflectance spectra. *Phil Mag* 88(5):781–794
25. Sipe JE, Young JF, Preston JS, Van Driel HM (1983) Laser-induced periodic surface structure I Theory. *Phys Rev B* 27(2):1141–1154
26. Her TH, Finlay RJ, Wu C, Mazur E (2000) Femtosecond laser-induced formation of spikes on silicon. *Appl Phys A* 70:383–385
27. Wu C (2000) Femtosecond laser-gas-solid interactions. Dissertation, Harvard University
28. Carey JE (2004) Femtosecond-laser microstructuring of silicon for novel optoelectronic devices. Dissertation, Harvard University
29. Kuo CC, Yeh WC, Chen JB, Jeng JY (2006) Monitoring explosive crystallization phenomenon of amorphous silicon thin films during short pulse duration XeF excimer laser annealing using real-time optical diagnostic measurements. *Thin Solid Films* 515:1651–1657
30. Elliq M, Fogarassy E, Stoquert JP, Fuchs C, Unamuno S, Preot B (1990) Pulsed excimer and Nd:YAG laser crystallization of a-Si:H—the specific role of hydrogen. *Appl Surf Sci* 46:378–382
31. Kruger J, Kautek W (1995) Femtosecond-pulse laser processing of metallic and semiconducting thin films. *SPIE* 2403:436–447
32. Kautek W, Rudolph P, Daminelli G, Kriger J (2005) Physico-chemical aspects of femtosecond-pulse-laser-induced surface nanostructures. *Appl Phys A* 81:65–70